State of health estimation for lithium-ion batteries based on temperature prediction and gated recurrent unit neural network

State of Health Estimation for Lithium-ion Batteries Based on Temperature Prediction and Gated Recurrent Unit Neural Network

Zheng Chen[1], Hongqian Zhao[1], Yuanjian Zhang[2], Shiquan Shen[1], Jiangwei Shen[1,**] and Yonggang Liu[3*]
[1]Faculty of Transportation Engineering, Kunming University of Science and Technology, Kunming, 650500, China
[2]School of Mechanical and Aerospace Engineering, Queen's University of Belfast, BT9 5AG, Northern Ireland
[3]State Key Laboratory of Mechanical Transmissions & College of Mechanical and Vehicle Engineering, Chongqing University, Chongqing, 400044, China
Email: chen@kust.edu.cn, zhaohongqian@stu.kust.edu.cn, y.zhang@qub.ac.uk, shenjiangwei6@163.com, andylyg@umich.edu
Corresponding author: Yonggang Liu (andylyg@umich.edu) and Jiangwei Shen (shenjiangwei6@163.com)

Abstract: Accurate state of health estimation for lithium-ion batteries is crucial to ensure the safety and reliability of electric vehicles. This study presents an accurate state of health estimation method based on temperature prediction and gated recurrent unit neural network. First, the extreme learning machine method is leveraged to forecast the entire temperature variation during the constant current charging process based on randomly discontinuous short-term charging data. Next, a finite difference method is employed to calculate the raw differential temperature variation, which is then smoothed by the Kalman filter. On this basis, multi-dimensional health features are extracted from the differential temperature curves to reflect battery degradation from multiple perspectives, and six strong correlated features are selected by the Pearson correlation coefficient method. After preparing all the related health features, the gated recurrent unit neural network is exploited to predict state of health. The feasibility of the developed method is verified by comparing with other classic approaches in terms of accuracy and reliability. The experimental results demonstrate that the proposed method can effectively lead to the error of state of health within 2.28% based on only partial random and discontinuous charging data, justifying its anticipated prediction performance.

Key Words: Lithium-ion battery, state of health, temperature prediction, differential temperature curve, gated recurrent unit neural network.

NOMENCLATURE

Abbreviations

EVs	electric vehicles	H	the measurement matrix
li-ion	lithium-ion	v	measurement noise

SOH	state of health
Ah	ampere-hour
BMSs	battery management systems
ECM	equivalent circuit model
EKF	extended Kalman filter
SEIKF	singular evolutive interpolated Kalman filter
KF	Kalman filter
HF	health feature
SVM	support vector machine
GPR	gaussian process regression
RVM	relevance vector machine
RF	random forest
NN	neural network
ELM	extreme learning machine
RNN	recurrent NN
LSTM	long short-term memory
GRU	gated recurrent unit
RUL	remaining useful life
ICA	incremental capacity analysis
DVA	differential voltage analysis
DTV	differential thermal voltammetry
CC	constant current
DT	differential temperature
SVR	support vector regression
TP	temperature prediction
BP	backward propagation
FNN	feedforward NN
MSE	mean square error
mAh	milli Ampere-hour
EOL	end of life
OCV	open circuit voltage
SOC	state of charge
RMSE	root mean square error
MAE	mean absolute error
MAX	max absolute error
PCC	Pearson correlation coefficient
R^2	R–squared

Symbols

$\hat{N}$	training set samples of ELM
α_i	input vector of ELM
R^n	the input vector of ELM is made up of n real numbers
γ_i	output vector of ELM
R^m	the output vector of ELM is made up of m real numbers
L	hidden neurons of ELM
Q	covariance of system noise
R	covariance of measurement noise
t	discrete time moment
P	error covariance
K	Kalman gain
r_t	outputs of the reset gate
z_t	outputs of the update gate
h_{t-1}	hidden state of the previous moment
x_t	the current input
σ	sigmoid function
W_r	weight matrices of reset gate
W_z	weight matrices of update gate
$\tilde{h}_t$	candidate hidden state
$tanh$	hyperbolic tangent function
W_h	weight matrices of temporary output
$\odot$	elementwise production
h_t	hidden state at current moment
y_t	output of the GRU NN
∂	linear activation function
W_o	weight matrices of output layer
b_o	bias corresponding to the output layer
N	length of the training time series
y^*	reference SOH
$C_{current}$	current capacity
C_{new}	nominal capacity
t_d	total discharging time
η	coulombic efficiency
$I(t)$	discharging current
τ	charging time
V_a	charging terminal voltage dataset
I_a	charging current dataset
SOC_a	charge SOC dataset
T_a	charge temperature dataset
V_i	charge terminal voltage at time i
I_i	charge current at time i
SOC_i	charge SOC at time i
T_i	charge temperature at time i
M	sampling interval
r	coefficient of PCC
$\bar{x}$	HFs mean
$\bar{y}$	SOH mean
$\hat{n}$	the number of DT curves
H_1	the height of the peak 1 of the DT curve
H_2	the height of the valley 2 of the DT curve

β_k	the weight vector connecting the *k*th hidden and the output neuron of ELM	H_3	the height of the peak 2 of the DT curve
$g(x)$	activation function of ELM	H_4	the height between peak 1 and valley 2 of the DT curve
ω_k	the weight vector concatenating the input and the *k*th hidden neuron of ELM	H_5	the height between valley 2 and peak 2 of the DT curve
b_k	the bias of the *k*th hidden neuron of ELM	V_B	the voltage of the peak 1 of the DT curve
$\mathbf{H}$	the hidden layer output matrix of ELM	V_C	the voltage of the valley 2 of the DT curve
$\hat{\beta}$	optimal β_k	V_D	the voltage of the peak 2 of the DT curve
$\mathbf{H}^+$	the Moore–Penrose generalized inverse matrix of $\mathbf{H}$	D_1	the distance between peak 1 and valley 2 of the DT curve
X	system state	D_2	the distance between valley 2 and peak 2 of the DT curve
A	the state change matrices	t_1	the time between valley 1 and peak 1 of the DT curve
w	system noise	t_2	the time between peak 1 and valley 2 of the DT curve
Y	measurement value	t_3	the time between valley 1 and peak 2 of the DT curve

I. INTRODUCTION

With the continuous aggravation of environmental pollution and energy crises, global automotive industry undergoes an unprecedented electrification revolution [1]. Electric vehicles (EVs) have become a promising option to alleviate greenhouse gas emission and promoting operation efficiency [2]. Lithium-ion (li-ion) batteries have been served as preferable energy sources in EVs due to the remarkable advantages including high energy/power density, high efficiency, wide operating temperature range, low self-discharge rate, long service lifespan and environmental friendliness [3]. However, the capacity of li-ion batteries gradually attenuates over repeated cycling operations with the format of loss of lithium inventory, decomposition of active material and loss of conductivity [4], thereby deteriorating the output capability. Thus, to improve battery performance and extend battery lifespan, state of health (SOH), as a crucial indictor of output capacity, needs to be elaborately investigated [5].

Currently, a large variety of SOH estimation methods have emerged, and these methods can be generally divided into three categories: direct measurement methods, model-based methods and data-driven methods. Ampere-hour (Ah) integration method is a representative manner among direct measurement methods, and has been widely applied in on-board battery management systems (BMSs) due to its simplicity and low computational complexity [6]. Unfortunately, the accumulated error and sensor noise will raise large deviations during estimation process, and these blemishes are untoward to mitigate. Other direct measurement approaches, such as ohmic

resistance measure and cycle number counting method [7], are only suitable for offline estimation since they can be easily influenced by operating temperature and load condition [8]. To alleviate the inherent shortcomings of previously addressed methods, model-based methods have gained a slew of attention and attained substantial progress [9]. Conventional solutions include equivalent circuit model (ECM) based method [10], electrochemical model based method [11] and empirical model based method [12]. The essence of these methods is to estimate SOH by leveraging prior knowledge of life degradation and the law of electrochemical reactions inside of batteries [13]. In ECM based method, the equivalent circuit components including capacitors and resistors are identified to highlight the battery's degradation behavior. In [14], two extended Kalman filters (EKFs) based on ECM are incorporated to calibrate SOC microscopically and update SOH macroscopically. Nonetheless, the parameter identification process is complicated and time-consuming, and the parameter variation law is highly nonlinear and difficult to identify [15]. Electrochemical model based method usually employs nonlinear partial differential equations to mimic battery's dynamic characteristics according to the electrical reaction and heat transfer mechanisms occurring inside of the batteries [16]. However, the electrochemical model without simplification requires intensive computations and many input parameters when solving a large number of partial differential equations [17]. To overcome this difficulty, Ref. [18] designs a simplified pseudo-two-dimensional model to characterize electrolyte dynamics and then calibrates SOH based on the prediction of average lithium concentration at the cut-off voltages during charging and discharging operations. In [19], an ensemble method based on singular evolutive interpolated Kalman filter (SEIKF) is addressed to efficiently enhance the adaptivity of battery estimator with degradation-conscious high-fidelity electrochemical-thermal model, and the ability to track the battery SOH variation is demonstrated. In empirical model based approach, exponential functions and reduced-order polynomial are usually hired to characterize battery's internal electrochemical dynamics [20]. Ref. [21] estimates battery life by an Arrhenius empirical model and further improves the estimation performance with the incorporation of Kalman filter (KF) and fuzzy logic. This method typically features high computational efficiency, while the accuracy can only be guaranteed under the similar operating conditions as that during model construction, leading to weak generalization ability and unfavorable robustness [22]. Moreover, the accuracy of model-based approaches highly relies on the fidelity of established models. It is not an easy task to construct a high-fidelity model to comprehensively characterize the aging dynamic behaviors in different operation conditions [23]. Furthermore,

these approaches also entail proper model simplification and efficient parameter identification before online implementations.

Data driven methods have been widely applied in SOH estimation, and they do not need to get insight into the complicated electrochemical reactions during model construction and SOH estimation. With the easy flexibility and superior nonlinear learning ability, these methods can effectively simulate the relationship between battery health feature (HF) and SOH without any understanding on inner electrochemical reaction. Ref. [24] reveals the efficiency of data driven modelling in predicting the behavior of complex dynamical systems and manifests that data driven method is a promising route for state estimation of li-ion batteries. According to the capacity degradation principle of li-ion batteries, one can know that obvious capacity degradation will undergo hundreds, or even more, of charge/discharge cycles, and the capacity degradation data can be considered as long-term time series sequence. From this point of view, SOH estimation can be regarded as a non-liner long-time series predicting problem [25]. Conventional data driven methods, including support vector machine (SVM) [26], Gaussian process regression (GPR) [27], relevance vector machine (RVM) [28], random forest (RF) [29] and neural network (NN) [30], are widely employed to forecast battery SOH. In [31], the SVM is leveraged to establish an efficient SOH estimation model, and the HFs are generated based on the impedance parameters. Ref. [32] proposes a GPR based network to estimate battery SOH using based on four HFs extracted from the charging curves. In [8], the voltage variance during a predefined time interval is considered as HF, and ELM is employed to estimate SOH. In [33], the increment of ohmic resistance and polarized resistance in the Thevenin model is utilized to correlate with the variation of SOH, and a metabolic ELM framework is mapping this nonlinear variation relationship. Nevertheless, these methods may not perform well as expected, since they usually assume that all the input variables are independent among each other and identically distributed [34], thus making them intractable to account for time series prediction. With the development of deep learning techniques, recurrent NN (RNN) exhibits convincible capabilities in processing time-series data, thanks to its specific self-feedback structure and functionalities in memorizing previous time sequence information. However, traditional RNN cannot handle long-term dependence due to gradient vanishing and gradient explosion problem. In this context, long short-term memory (LSTM) NN and gated recurrent unit (GRU) NN are advanced to tackle the shortcomings of traditional RNN. Both methods exploit special gated structures to control the information flow thus ensuring the normal variation of gradient [35]. Ref. [36] successfully leverages the LSTM

NN to establish a degradation model based on real-time operation data. Ref. [37] extracts six HFs from the charging and discharging processes, and a dynamic spatial and temporal attention-based GRU NN is introduced for SOH estimation. Ref. [38] combines transfer learning and GRU NN to estimate remaining useful life (RUL) based on the HFs extracted from partial voltage curves during fast charging operations. As widely known, LSTM unit consists of forget gate, input gate and output gate, and can control useful information transfer. Moreover, GRU unit is a simplified form of LSTM unit that includes update gate and reset gate, which can be leveraged to determine what information can pass [39]. Compared with LSTM unit, GRU unit features simpler structure and fewer parameters, thereby improving the efficiency of network training and prediction. Ref. [40] shows that GRU NN is more qualified than LSTM NN in embedded implementation. Based on these discussions, GRU NN is continuously employed in this study to predict the battery SOH.

In addition, to attain efficient SOH estimation based on data driven methods, a pivotal process is HF extraction. In the existing HF extraction schemes, incremental capacity analysis (ICA) [41] and differential voltage analysis (DVA) [42] are two representative methods. Ref. [4] presents the ICA method for battery SOH estimation based on grey relational analysis and entropy weight method. In [43], the battery SOH is estimated according to the inflection point position and transformation parameters of differential voltage curve. It is worth noting that these HF extraction methods rely mainly on voltage characteristics, and rarely consider temperature variation during battery degradation. Ref. [44] verifies that temperature variation is efficient to quantify the aging process of li-ion batteries. Ref. [45] generates differential thermal voltammetry (DTV) curves via differentiating the measured temperature over voltage during the constant current (CC) charging phase. However, the DTV easily suffers from noise interference. Moreover, these HF generation methods usually require full charging data; however, it is difficult, and even impossible, to acquire the entire charging data in practice. To solve these problems, Ref. [46] excavates differential temperature (DT) curves in a fixed voltage region during the charging process to estimate SOH by support vector regression (SVR). However, to extract HFs in a fixed voltage range, the battery needs to be charged across the initial and terminal threshold of the selected voltage range. While battery charging behavior tends to be a random process since end-users may start and stop charging randomly. Moreover, due to the sampling error and measure interference, data loss often occurs during acquisition. From this point of view, SOH estimation through directly measuring the complete charging data or fixed voltage region data is usually impractical in real-time applications.

To overcome this bottleneck, this study proposes a SOH estimation method based on partial random charging data and battery surface temperature. First, a temperature prediction (TP) model based on ELM is developed to compensate the missing sector of temperature variation using only partial random and discontinuous charging data, in case that the temperature curve is not complete. Then, multi-dimensional HFs are extracted from DT curves to sketch battery degradation from multiple perspectives. Third, considering the long-term time series peculiarity of battery degradation behavior, GRU NN, which is with less parameters and simpler structure than traditional RNN and LSTM, is leveraged to estimate battery SOH. The experimental results demonstrate that the proposed approach can efficiently lead to precise SOH estimation with the error of less than 2.28%, justifying its anticipated prediction performance. From the validation process, we can find that the proposed method requires only partial random and discontinuous charging data and enables precise SOH estimation. The main contributions of this paper added to the literature can be summarized as follows.

1) A TP model based on ELM is advanced to compensate the missing sector of temperature variation information using only partial random and discontinuous charging data.

2) Multi-dimensional HFs are extracted from DT curves to elaborate battery degradation from different perspectives, and GRU NN is leveraged to estimate battery SOH efficiently.

The remaining content of this paper is structured as follows. Section II introduces the fundamental principle of ELM, KF and GRU NN. Section III details the aging datasets and establishes the TP model. Section IV elaborates the DT curve calculation, HFs extraction and selection as well as the SOH estimation procedure. Next, the estimation performance of the proposed method is evaluated in Section V. Finally, the conclusions are drawn in Section VI.

II. METHODOLOGY

This section describes the principles and derivations of related algorithms applied for SOH estimation, including ELM, KF and GRU NN.

A. Extreme Learning Machine Algorithm

Traditional NN learning algorithms such as backward propagation (BP) NN need to manually set network parameters, and their iterative process based on gradient descent shows a slow convergence speed and can easily fall into local optimum [47]. To surpass these shortcomings, Ref. [48] designs the ELM algorithm, which is a brand-

new framework of feedforward NN (FNN) learning and developed from single-hidden layer feedforward NN. The ELM algorithm does not need to adjust the input weight of network and the bias of hidden neurons during implementation. By means of the Moore-Penrose generalized inverse operation, the output weight of ELM can be solved based on the minimization of square loss function. Thus, the minimum norm least square solution can be obtained to reach optimization. Moreover, in ELM algorithm, only the number of hidden neurons needs to be adjusted, and multiple iterations can be avoided, thus reducing the computational intensity. In short, ELM algorithm features the advantages of simple implementation, fast learning speed and easy implementation. Given a training set containing $\hat{N}$ samples $\{(\alpha_i, \gamma_i)\}_{i=1}^{\hat{N}}$, where $\alpha_i \in R^n$ represents the input vector and $\gamma_i \in R^m$ denotes the corresponding expected output vector, the output of ELM with L hidden neurons can be formulated, as:

$$\gamma_j = \sum_{k=1}^{L} \beta_k g(\omega_k \cdot \alpha_j + b_k), \quad j = 1, 2, \ldots, \hat{N} \tag{1}$$

where $g(x)$ denotes activation function, $\omega_k = [\omega_{k1}, \omega_{k2}, ..., \omega_{kn}]^T$ is the weight vector concatenating the input and the *k*th hidden neuron, b_k refers to the bias of the *k*th hidden neuron, $\beta_k = [\beta_{k1}, \beta_{k2}, ..., \beta_{km}]^T$ represents the weight vector connecting the *k*th hidden and the output neuron. As such, equation (1) can be can be reformulated, as:

$$\mathbf{H}\beta = \boldsymbol{\gamma} \tag{2}$$

where $\beta = [\beta_1, \beta_2, ..., \beta_L]^T$, $\boldsymbol{\gamma} = [\gamma_1, \gamma_2, ..., \gamma_{\hat{N}}]^T$, and $\mathbf{H}$ denotes the hidden layer output matrix, as:

$$\mathbf{H} = \begin{bmatrix} g(\omega_1 \cdot \alpha_1 + b_1) & \cdots & g(\omega_L \cdot \alpha_1 + b_L) \\ \vdots & \cdots & \vdots \\ g(\omega_1 \cdot \alpha_{\hat{N}} + b_1) & \cdots & g(\omega_L \cdot \alpha_{\hat{N}} + b_L) \end{bmatrix} \tag{3}$$

Then, the optimal $\hat{\beta}$ can be deduced, as:

$$\hat{\beta} = \mathbf{H}^{+}\boldsymbol{\gamma} \tag{4}$$

where $\mathbf{H}^{+}$ denotes the Moore–Penrose generalized inverse transformation of $\mathbf{H}$, and the generalization performance can be achieved by singular value decomposition. Based on the above analysis, this study adopts ELM algorithm to establish the TP model of li-ion batteries. Next, the KF algorithm will be introduced.

B. KF Algorithm

KF algorithm has achieved substantial applications in the fields of signal processing, system control and computer application. KF is an optimal recursive data processing algorithm using the minimum mean square error as the optimal criterion, and can remove the noise in data stream without distorting the signal tendency [49]. The linear time-varying discrete system can be expressed as:

$$\begin{cases} X_t = AX_{t-1} + w_{t-1} \\ Y_t = HX_t + v_t \end{cases} \tag{5}$$

where X denotes the system state; Y stands for the measurement value; A and H represent the coefficient matrices; w means the system noise with the covariance of Q; v is the measurement noise and its covariance is R. The subscript t denotes the t th discrete time step. The general process of KF algorithm is illustrated in Table 1, and includes three key steps: initialization, time update and measurement update. In this study, KF algorithm is implemented to smooth the DT curves. In the next step, a brief introduction of GRU NN is investigated.

Table 1 The Executing Processes of KF Algorithm

Step1: Initialization: for $t=0$, set $\hat{X}_0^+$, P_0^+, Q, R
Step2: Time update: for $t=1,2,...,$ calculate
Prior estimate of state: $\hat{X}_t^- = A\hat{X}_{t-1}^+$
Prior estimate of error covariance: $P_t^- = AP_{t-1}^+A^T + Q$
Step3: Measurement update:
Kalman gain matrix update: $K_t = P_t^- H^T (HP_t^- H^T + R)^{-1}$
Measurement update of state estimate: $\hat{X}_t^+ = \hat{X}_t^- + K_t(Y_t - H\hat{X}_t^-)$
Measurement update of error covariance: $P_t^+ = P_t^- - K_t HP_t^-$
Step 4: Time update: return to Step 2

C. GRU NN

The structure of a typical GRU NN, as shown in Fig. 1 (a), consists of an input layer, a hidden layer, and an output layer. The architecture diagram of GRU unit is displayed in Fig. 1 (b), which includes the reset gate r_t and the update gate z_t, and they are determined by the previous hidden state h_{t-1} and the current input x_t. The forward propagation process of GRU NN can be formulated, as:

$$\begin{cases} r_t = \sigma\left(W_r \cdot \left[h_{t-1}, x_t\right]\right) \\ z_t = \sigma\left(W_z \cdot \left[h_{t-1}, x_t\right]\right) \\ h_t = tanh\left(W_h \cdot \left[r_t \odot h_{t-1}, x_t\right]\right) \\ h_t = \left(1 - z_t\right) \odot h_{t-1} + h_t \odot z_t \\ y_t = \partial(W_o h_t + b_o) \end{cases} \tag{6}$$

where σ and *tanh* denote the activation function; σ means the sigmoid function; *tanh* is the hyperbolic tangent function; ∂ is the linear activation function. $\odot$ refers to the elementwise production. W_r, W_z, W_h and W_o are the weight matrices of the reset gate, update gate, temporary output, and output layer, respectively. b_o is the bias corresponding to the output layer. r_t means the outputs of the reset gate, and z_t denotes the outputs of the update gate. $\tilde{h}_t$ and h_t are the candidate hidden state and the hidden state, respectively. y_t represents the output of the GRU NN. During the training process, the mean square error (MSE) is considered as the loss function of GRU NN:

$$MSE = \frac{1}{N}\sum_{t=1}^{N}(y_t - y_t^*)^2 \tag{7}$$

where N denotes the length of the training time series, and y^* is the reference value of y.

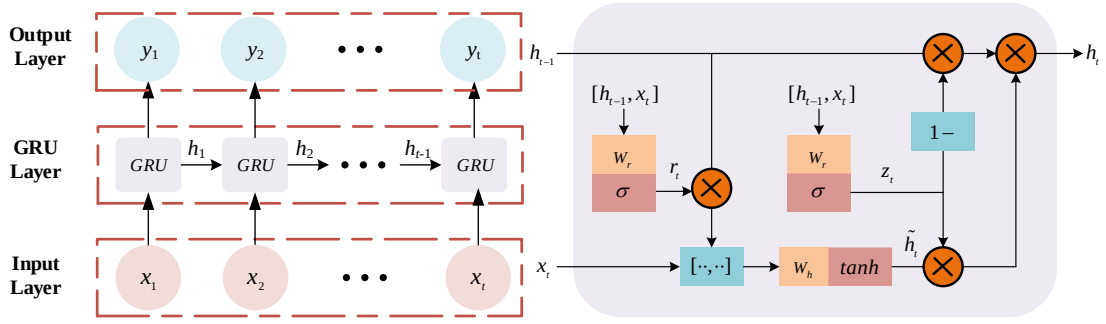

(a) (b)

Fig. 1. The structure of GRU NN and GRU unit. (a) Structure of GRU NN. (b) Structure of GRU unit.

Considering the advantages of GRU NN, this study chooses a deep learning architecture constructed by GRU NN to estimate SOH. Note that the activation function in the output layer is a linear function. As widely known, in NNs, activation functions are quite significant, as they are critical during learning and understanding the mapping relationships between the inputs and corresponding outputs. Generally, the activation functions are mainly divided into linear types and nonlinear ones. Linear activation functions are simpler and easier to solve questions, compared with nonlinear activation functions [50]. Since the estimation of SOH is a regression problem, and the output layer

does not need to cope with complicated nonlinear mappings, the linear activation function is selected as the activation function. Moreover, to prevent over-fitting and promote the generalization ability of the network, the dropout technique is adopted, which can drop neurons randomly from the network during training, resulting in less sensitivity of the network to the specific weights of neurons [51]. Additionally, the Adam optimization algorithm is introduced for model training, and is, to now, the most common gradient-based algorithm to optimize loss functions due to the ability of adaptive learning rate calculation and less storage requirements [52]. In the next step, the preparation of feature extraction, including battery aging test and TP model, will be elaborated.

III. Experiment Discussion and Temperature Prediction

This section will detail the aging test and elaborate the process of TP based on only partial charging data.

A. Aging Experiment

In our study, a public dataset published by the University of Oxford is imported for algorithm analysis [53]. As introduced in [53], the battery experiment platform involves a thermal chamber, an 8-channel battery tester and a host computer. The test batteries include eight commercial Kokam pouch cells (called cells 1 to 8 hereinafter) with the rated capacity of 740 milli Ampere-hour (mAh). The operation voltage of these cells ranges from 2.7 V to 4.2 V. The anode material of the test cells is graphite, and the cathode is a mixture of lithium cobalt oxide and lithium nickel cobalt oxide. As we all know, li-ion battery is an electrochemical power source, its action process depends on the ability of electrochemical reaction, and the temperature determines the activity degree of most chemical reaction processes. In the case of high temperature, the adverse reaction inside of the battery is intensified, and the reaction between electrolyte and anode materials consumes more materials and lithium ions, resulting in the accelerated decay of capacity. Thus, the cycle aging speed of battery at high temperature is faster than that at room temperature [54]. On this account, an elevated test temperature (40℃) experiment is selected to accelerate the aging process of the cells. As shown in Table 2, the battery cycle test consists of characterization test, driving cycle test and end of life (EOL) judgment. In driving cycle test, all the cells are charged with 2 C (C denotes the value of the rated capacity) current until the voltage reaches 4.2 V, and discharged according to the Artemis urban driving profile to emulate the actual driving conditions of EV until the voltage drops to 2.7 V. After 100 drive cycles, a characterization test is performed, and the data including time, voltage, charge and temperature is recorded by the

battery tester. The sampling interval for the characterization test is 1 s, and more detailed experimental description can be found in [53]. In the characterization test, the battery is charged and discharged with 1 C current to calibrate its current capacity. The data in this process are utilized for model construction. To be specific, the charging data is employed to extract HFs and the discharging data accounts for the reference capacity calculation. The battery capacity in this study is calculated by integrating the discharge current at the end of each recorded discharging cycle. Then, the reference SOH can be calculated as,

$$\begin{cases} C_{current} = \int_0^{t_d} \eta I(t) dt \\ SOH = C_{current} / C_{new} \end{cases} \tag{8}$$

where $C_{current}$ and C_{new} represent the current capacity and nominal capacity of the test battery, respectively; t_d denotes the total discharging time; η is the coulombic efficiency; and $I(t)$ means the discharging current. A typical definition is that the EOL threshold for li-ion batteries is that the current capacity reaches 80% of the rated value; that is, when the SOH decreases to 80%, the batteries are supposed to be abandoned or recycled [55]. Therefore, we only selected the data with SOH higher than 80% as our research object. Taking cell 1 as an example, in the raw data, a total of 8,200 driving cycles are conducted, and SOH decreased to 75.9%. When the number of driving cycles is 5,100, SOH is 79.8%. Therefore, we only selected the first 5,000 driving cycle data to conduct SOH analysis. Since a characterization test is performed every 100 drive cycles, 50 cycle curves of cell 1 can be utilized for SOH estimation.

Table 2 Test schedule of the Oxford Dataset

Stage 1: Characterization test
(a) 1 C test: Charge and discharge with 1 C (740 mA) current.
(b) Pseudo-OCV test: Charge and discharge with C/18.5 (40 mA) current.
Stage 2: Drive cycle (repeat 100 times)
Charge the battery with 2 C (1480 mA) current and discharge the battery with the Artemis Urban driving profile (average current =1.36 A).
Stage 3: End of life (EOL) judgment
If the cell fails or loses at least 20% of its rated capacity, end the test; otherwise, repeat stages 1 and 2 experiment.

B. TP Model

During the daily use of EVs, to avoid range anxiety, end-users usually limit batteries operation within a proper range, and batteries have little opportunities for full discharge. Furthermore, battery discharging process is usually stochastic and unpredictable, leading to difficulty in extracting suitable HFs. By contrast, the charging process is

more regular and more uniform, as the battery is usually charged from the power grid according to specific instructions [56]. On this account, the electrical characteristics during the charging process is investigated to design HFs. However, due to the sampling error and measure interference, data loss often occurs in the process of acquisition. To compensate the incomplete information of temperature variation profile, this study designs a TP model based on the ELM to predict the entire charging temperature curve. The ELM algorithm, which features anti-noise functionality, fast learning speed and strong generalization performance, is exploited to predict temperature variation. According to the study in [57], the battery temperature is related to current, internal resistance and open circuit voltage (OCV). From the perspective of parameter identification, battery impedance is highly related to state of charge (SOC) and terminal voltage, and OCV is correlated with SOC. Consequently, terminal voltage, current and SOC in partial time charging process are regarded as the input of ELM to acquire whole charging temperature variation curve. Concretely, we assume that the battery is charged for a short time τ, and the recorded terminal voltage, current, SOC and temperature, referred to as V_a, I_a, SOC_a and T_a, are collected from beginning to the present moment. In short, we can summarize that the input vector can be denoted as $\alpha_i = [V_i \ I_i \ SOC_i]$, and the output vector is expressed as $\gamma_i = [T_i]$, where the subscript i denotes the ith time step, and γ_i is the actual temperature corresponding to α_i.

As described in Section II, only one parameter needs to be tuned in the ELM model. Here, the effect of hidden neurons number on the TP model performance is evaluated based on the indicators including root mean square error (RMSE), mean absolute error (MAE), max absolute error (MAX) and running time. Fig. 2 demonstrates the RMSE, MAE, MAX and running time based on the training dataset, which is set with the same length (70% of the charging data are randomly selected). As can be seen from Fig. 2, when the neuron is less than 14, not only is the model error relatively large, but also the error fluctuates obviously. This is because the potential nonlinear dynamic relationship between model input and output cannot be learned by limited neurons. As the number of neurons increases from 14 to 21, the RMSE, MAE and MAX showcase a decreasing trend. However, when the number of neurons exceeds 21, the performance of TP model does not increase obviously; however, the running time increases gradually. Thus, the number of neurons for ELM algorithm is set to 21 by trading-off learning ability and efficiency.

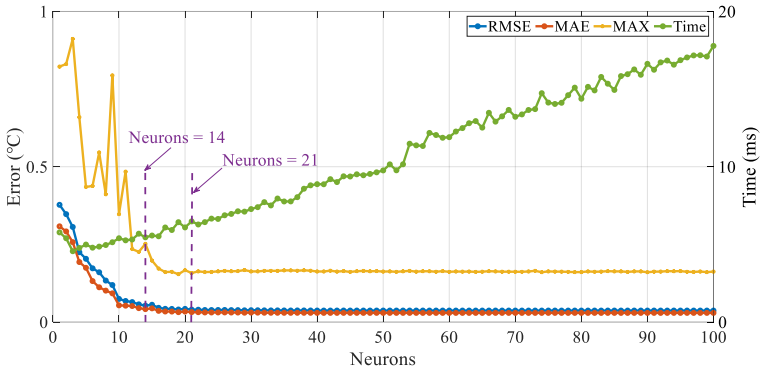

Fig. 2. The result of ELM with different hidden neurons.

Based on the well-designed TP model, the complete temperature curves for all the cells in the charging process can be generated. Fig. 3 (a) and (b) show the measured temperature variation profiles and that based on TP for cell 1. There exist 50 cycle curves in Fig. 3, and the reason for the curve discontinuity lies in that the characterization test is conducted every 100 cycles during the test. The results show that the general shape outputted by the ELM model is highly consistent with the measurement, and the predicted curves are smoother than those from raw measurement and thus conducive to the extraction of HFs. Table 3 illustrates the minimum and maximum of RMSE, MAE and MAX for each cell. As can be found, the RMSE is mainly distributed within 0.0340 ℃ and 0.0400 ℃, the MAE ranges from 0.0270 ℃ to 0.0321 ℃, the range of the MAX is mostly located within 0.1150 ℃ to 0.4370 ℃, and the maximum MAX is less than 0.5000 ℃, manifesting that the proposed TP method can efficiently provide accurate and reliable temperature prediction results. As can also be found, with the increase of cycle number, the temperature curves shift upward and vary dramatically. From this point of view, battery temperature variation curves during the charging process has a strong correlation with SOH and can be hired as a valuable index to quantify SOH variation, and the specific HFs extraction method and SOH estimation process will be introduced in the next section.

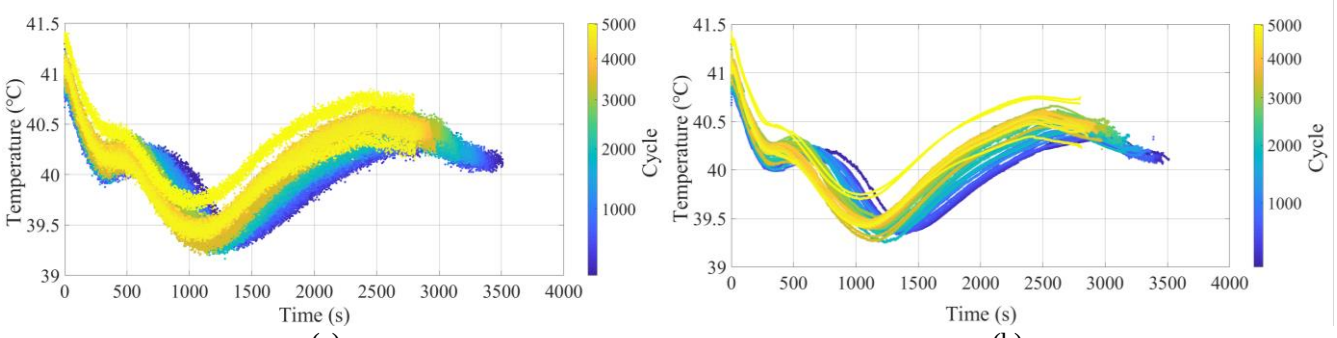

Fig. 3. TP results for cells 1. (a) Raw temperature curves. (b) TP curves.

Table 3 TP results of cell 1 to 8

cell	RMSE (℃)		MAE (℃)		MAX (℃)	
	Minimum	Maximum	Minimum	Maximum	Minimum	Maximum
1	0.0356	0.0400	0.0284	0.0319	0.1179	0.2253
2	0.0356	0.0394	0.0285	0.0316	0.1178	0.2889
3	0.0355	0.0399	0.0281	0.0316	0.1152	0.2162
4	0.0353	0.0400	0.0281	0.0318	0.1150	0.2414
5	0.0360	0.0399	0.0287	0.0321	0.1230	0.4072
6	0.0357	0.0400	0.0285	0.0317	0.1213	0.2373
7	0.0348	0.0398	0.0278	0.0318	0.1164	0.4367
8	0.0357	0.0400	0.0285	0.0318	0.1183	0.2172

IV. State of Health Estimation

In this section, the DT curves are obtained based on the TP results, and the noise is filtered by the KF algorithm. Then, the HFs are extracted. Additionally, the whole framework of SOH estimation for li-ion batteries is presented.

A. DT Curve Calculation

This study considers the temperature change in the battery degradation process, and the DT curve method is employed to analyze the deterioration characteristics of li-ion batteries. The DT curve describes the variation rate of temperature during the charging process. Although the predicted temperature curves follow the trend of the original temperature curves and show more smooth characteristics, the noise interference cannot be escaped in the measure process, and will affect the fidelity of DT curves. To alleviate it, finite difference method is usually employed to calculate the DT curves, as:

$$DT_t^* = \frac{dT_t}{dt_t} \approx \frac{T_t - T_{t-M}}{M} \tag{9}$$

where M refers to the sampling interval. Smaller M will lead to more noisy DT curve, and by contrast, larger M will raise weaker HF variation. M is set to 20 after trading-off the precision and sensitivity of temperature variation. The original DT curves of cell 1 are sketched in Fig. 4 (a) with the input of terminal voltage. As can be observed, these curves are full of noises, and it remains challenging when refining the DT curves to signify the aging variation of li-ion batteries. To solve it, the KF algorithm is exploited to improve the quality of DT curves. The smoothed value of DT is regarded as a state polluted by random noise, and the linear discrete system is expressed as:

$$\begin{cases} DT_t = DT_{t-1} + w_{t-1} \\ DT_t^* = DT_t + v_t \end{cases} \tag{10}$$

where DT_t and DT_t^* denote the system sate and measurement value, w and v represent the system noise and the measurement noise, respectively. Accordingly, the parameters in (5) can be determined, as: $X_t = DT_t$, $Y_t = DT_t^*$, $A = 1$ and $H = 1$. Based on the KF algorithm, the DT curves can be smoothed, as outlined in Fig. 4 (b), making it easier to extract effective HFs.

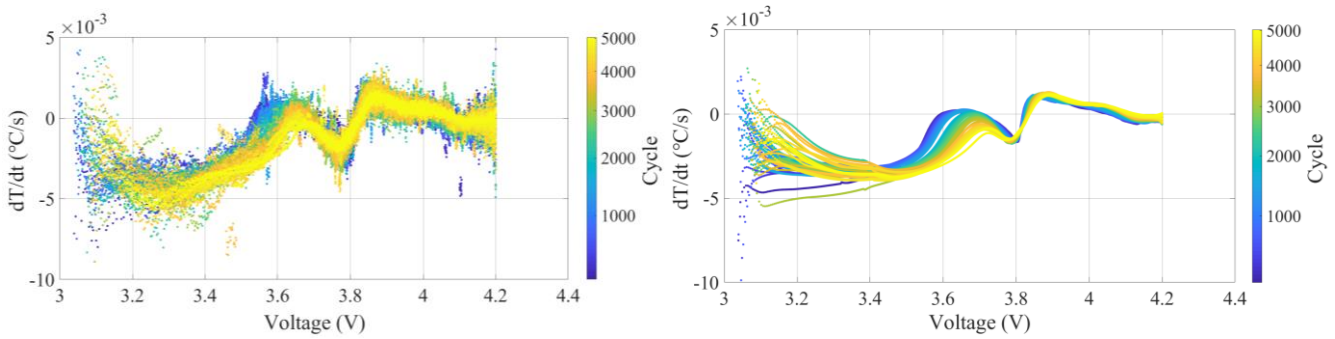

Fig. 4. DT curves of cell 1. (a) The raw DT curves. (b) The smoothed DT curves.

B. HFs Extraction and Selection

The extraction and selection of HFs are essential during SOH prediction. As describe above, we only need to obtain partial random data in the charging process, and then the complete temperature curve can be obtained through the established TP model based on the ELM algorithm. On this basis, it is quite easy to calculate DT curves and extract significant HFs. In practical applications, the primary operation voltage range of li-ion batteries is usually located within 3.2 V to 4.0 V [45]. One example of HFs extraction based on the DT curve is presented in Fig. 5, where thirteen HFs, including peak/valley height (H_1 to H_5), peak/valley voltage (V_B, V_C and V_D), the distance between peak and valley (D_1 and D_2) and the duration between peak and valley (t_1 to t_3), are firstly extracted from the DT curve. Then, to reduce the computational burden while maintaining the estimation precision, the Pearson correlation coefficient (PCC) is introduced to screen high correlational HFs that are served as the input of SOH prediction model. It is worth noting that the PCC value is located within [-1, 1], and its absolute value equaling 1 indicates an ideal linear correlation between two physical quantities. On the contrary, when the value equals 0, we can say that no linear correlation exists between two variables. The PCC can be formulated, as:

$$r = \frac{\sum_{t=1}^{\hat{n}} (x_t - \bar{x})(y_t - \bar{y})}{\sqrt{\sum_{t=1}^{\hat{n}} (x_i - \bar{x})^2} \sqrt{\sum_{t=1}^{\hat{n}} (y_t - \bar{y})^2}} \tag{11}$$

$$\bar{x}=\frac{1}{\hat{n}}\sum_{t=1}^{\hat{n}}x_t,\bar{y}=\frac{1}{\hat{n}}\sum_{t=1}^{\hat{n}}y_t \tag{12}$$

where $\hat{n}$ indicates the number of DT curves, x_t and y_t mean the HFs and SOH in each cycle number t, $\bar{x}$ represents the HFs mean value, and $\bar{y}$ is the SOH mean value. The PCC values of the thirteen HFs and eight cells are tabulated in Table 4. As can be found, the absolute values of PCC of V_B, V_D, H_1, H_4, t_2 and t_3 of eight cells are all greater than 0.80, highlighting that these six HFs are strongly correlated with SOH. Consequently, they are selected as the inputs of GRU model in this study, and the specific descriptions of these six HFs can be expressed as:

$$\begin{cases} V_B = V_{peak1} \\ V_D = V_{peak2} \\ H_1 = DT_{peak1} \\ H_4 = DT_{peak1} - DT_{valley2} \\ t_2 = t_C - t_B \\ t_3 = t_D - t_A \end{cases} \tag{13}$$

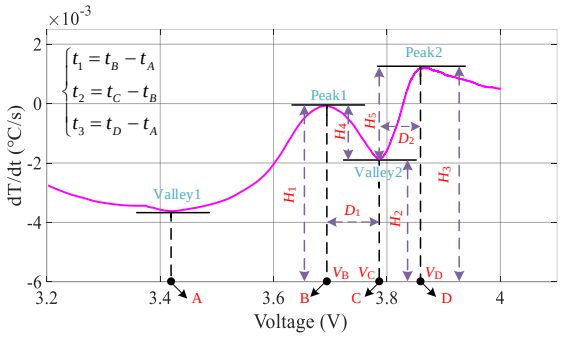

Fig. 5. Graphical illustration of the HFs on a DT curve.

Table 4 Correlation Analysis Results

HFs	cell 1	cell 2	cell 3	cell 4	cell 5	cell 6	cell 7	cell 8
V_B	0.95	0.94	0.93	0.84	0.88	0.94	0.93	0.95
V_C	0.73	0.11	0.69	0.90	0.88	0.91	0.60	0.69
V_D	-0.98	-0.97	-0.98	-0.97	-0.94	-0.97	-0.99	-0.98
H_1	-0.98	-0.97	-0.98	-0.99	-0.98	-0.98	-0.98	-0.97
H_2	-0.73	-0.09	-0.61	-0.29	0.60	-0.52	0.46	-0.44
H_3	-0.38	-0.15	-0.30	-0.35	-0.66	-0.35	-0.81	-0.56
H_4	0.95	0.95	0.93	0.94	0.80	0.93	0.93	0.95
H_5	0.39	-0.03	0.30	0.23	-0.66	0.16	-0.64	-0.01
D_1	0.87	0.60	0.85	0.95	0.95	0.96	0.91	0.85
D_2	-0.90	-0.67	-0.91	-0.96	-0.95	-0.96	-0.96	-0.91
t_1	0.59	0.49	0.81	0.94	0.95	0.93	0.93	0.85
t_2	0.98	0.96	0.97	0.99	0.98	0.99	0.98	0.97
t_3	0.94	0.93	0.85	0.92	0.90	0.94	0.82	0.87

C. SOH Estimation

The entire implementation procedure of SOH estimation based on the TP and GRU NN is illustrated in Fig. 6. The whole process is mainly divided into six steps: data acquisition, TP model training, DT variation solving and subsequent filtering, HFs extraction and selection, GRU NN training, and SOH estimation. When the entire charging temperature curve cannot be measured, the ELM will be activated, and then a whole DT can be obtained. In the next step, the KF algorithm is employed to smooth the DT curve. Subsequently, HFs are extracted, and the SOH estimation model based on GRU NN is constructed to excavate the veiled dependence between the selected HFs and SOH.

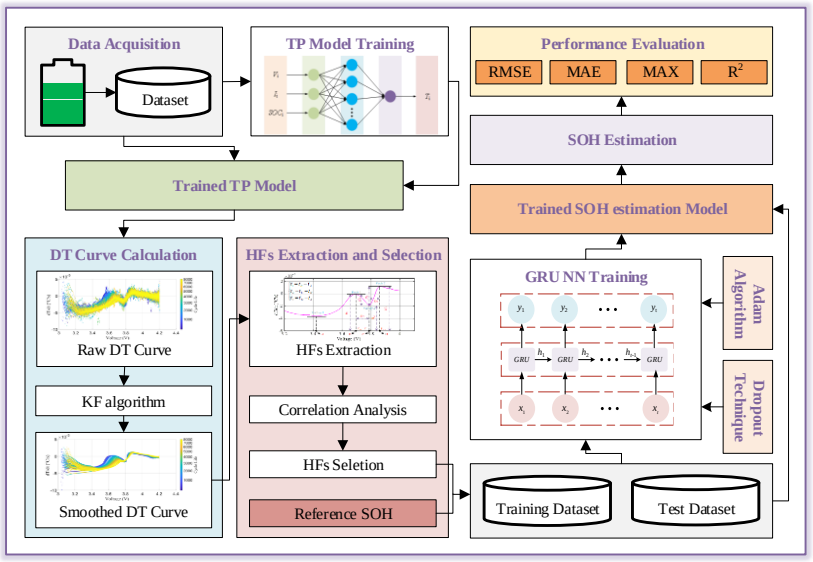

Fig. 6. The entire procedure of the SOH estimation.

In the following section, the estimation performance of the proposed method will be examined and discussed.

V. Results and Discussion

In this section, five critical hyper-parameters of the GRU model are firstly determined, and then the performance and feasibility of the proposed method based on the leave-one-out validation scheme are examined. Finally, the proposed method is compared with the commonly employed SOH prediction methods. In addition to RMSE, MAE and MAX, R-squared (R^2) is also engaged in appraising the estimation performance.

A. Hyper-Parameter Determination

The SOH prediction performance highly depends on the topology of GRU NN; that is, the setting of the hyper-parameters can generate significant influences on prediction performance. Theoretically, simpler GRU model leads to poorer learning and worse undesired underfitting; and instead, too complex GRU model can incur heavier

calculation burden and lower generalization ability. As such, the optimization of hyper-parameters in GRU model is the premise for accurate SOH estimation. Here, the data of cell 1 is employed for model validation, and the remaining cells' data accounts for model training. The hyper-parameters including hidden layer, neurons in each hidden layer, batch size, dropout rate and epoch are initially set to 1, 32, 64, 0.4 and 100.

The evaluation performances of the GRU model with different hyper-parameters are shown in Table 5. The least RMSE, MAE and MAX are distinguished as bold characters for clearer comparison. To be specific, we first conduct training based on 1 to 4 hidden layers, and the other hyper-parameters remain the same. It can be seen from Table 5 that when the number of the hidden layer is 2, the SOH prediction accuracy is highest, and when the neuron amount in each hidden layer is 60, the optimal estimation results are gained. Thus, the number of hidden layer and neurons in each hidden layer is fixed at 2 and 60, and the estimation results of different batch size are compared. Here, the batch size is set to128, 64, 32 and 16, respectively. As can be seen, three indexes including RMSE, MAE and MAX reach the minimum value simultaneously when the batch size equals 32. Thus, the batch size equaling 32 is determined. Next, according to the determined values of the hidden layer, the neurons in each hidden layer and batch size, the effects of different dropout rates on the model performance are compared. It can be known that the dropout rate equaling 0.4 leads to the optimal estimation results. Finally, from Table 5, no matter that epoch increases to 150 or decreases to 50, the RMSE, MAE and MAX all show an increasing trend, meaning that the performance of the model is not improved by modifying the epoch amount, and thus the epoch remains consistent with the initial value. To summarize, the structure of GRU model is determined, which includes 2 hidden layer and 60 neurons in each hidden layer. Moreover, the batch size, dropout rate and epoch are respectively set to 32, 0.4 and 100. On this basis, the RMSE, MAE and MAX of the SOH estimation can be restricted within 0.58%, 0.47% and 1.28%, respectively.

B. Leave-One-Out Validation

To verify the generalization of the proposed SOH method based on TP, the leave-one-out validation scheme is performed. Thereinto, the data of each cell are adopted as one test dataset, while the data of the residual seven cells constitutes the training dataset. Since the testing dataset does not appear in the training dataset, the trained GRU model features the ability of unbiased estimation. The verification process is repeated for eight times until each cell

is applied for model test. Moreover, the SOH estimation results based on raw complete temperature data are conducted to exhibit the reliability of the proposed method.

Table 5 Hyper-parameters Selection for SOH Estimation Model

Experiment number	Hyper-parameters					RMSE (%)	MAE (%)	MAX (%)
	Hidden layer	Neurons in hidden layer	Batch size	Dropout rate	Epoch			
1	1	32	64	0.4	100	1.13	0.91	2.87
2	2	32	64	0.4	100	0.60	**0.47**	1.82
3	3	32	64	0.4	100	0.69	0.54	1.74
4	4	32	64	0.4	100	0.74	0.66	1.55
5	2	16	64	0.4	100	0.72	0.54	2.2
6	2	60	64	0.4	100	0.59	0.51	1.23
7	2	64	64	0.4	100	0.65	0.51	1.57
8	2	64	128	0.4	100	0.59	0.49	1.40
9	2	60	32	0.4	100	**0.58**	**0.47**	**1.28**
10	2	60	16	0.4	100	0.68	0.55	1.59
11	2	60	32	0.5	100	0.66	0.51	1.66
12	2	60	32	0.3	100	0.77	0.60	1.80
13	2	60	32	0.2	100	0.68	0.58	1.35
14	2	60	32	0.1	100	1.00	0.84	2.16
15	2	60	32	0.4	50	0.79	0.69	1.85
16	2	60	32	0.4	150	0.80	0.65	1.87

Fig. 7 demonstrates the estimation results of cells 1, 3, 5 and 7, and the estimation error of cell 7, where SOH with TP represents the SOH estimation values obtained by the GRU NN with TP, and SOH without TP means the SOH estimation values acquired by the GRU NN with raw complete temperature data. Note that compared with the proposed method, only the TP process is omitted in SOH estimation based on raw entire temperature data, and the rest processes are kept the same. It can be clearly observed that the estimated SOH curves can effectively track the reference, and the MAX for all cells is mostly confined within 2%. The RMSE, MAE, MAX and R^2 are calculated and elucidated in Table 6. To assess the overall performance, Table 6 also summarizes the average estimation of eight cells. As can be seen, the RMSE, MAE and MAX based on TP are limited within 1.20%, 1.02% and 2.28%, respectively. The RMSE, MAE and MAX based on the raw complete temperature data is less than 1.14%, 0.95% and 2.41%. From the overall results, partial estimation errors based on TP are slightly larger than that with the raw complete temperature data, and this is incurred by the TP error on feature parameter extraction. However, the average values of R^2 for the two methods remain mostly the same. As such, it can be concluded that the estimation accuracy with TP is comparable to that of the method with raw complete temperature data. By this manner, the feasibility of the proposed method based on TP model is justified.

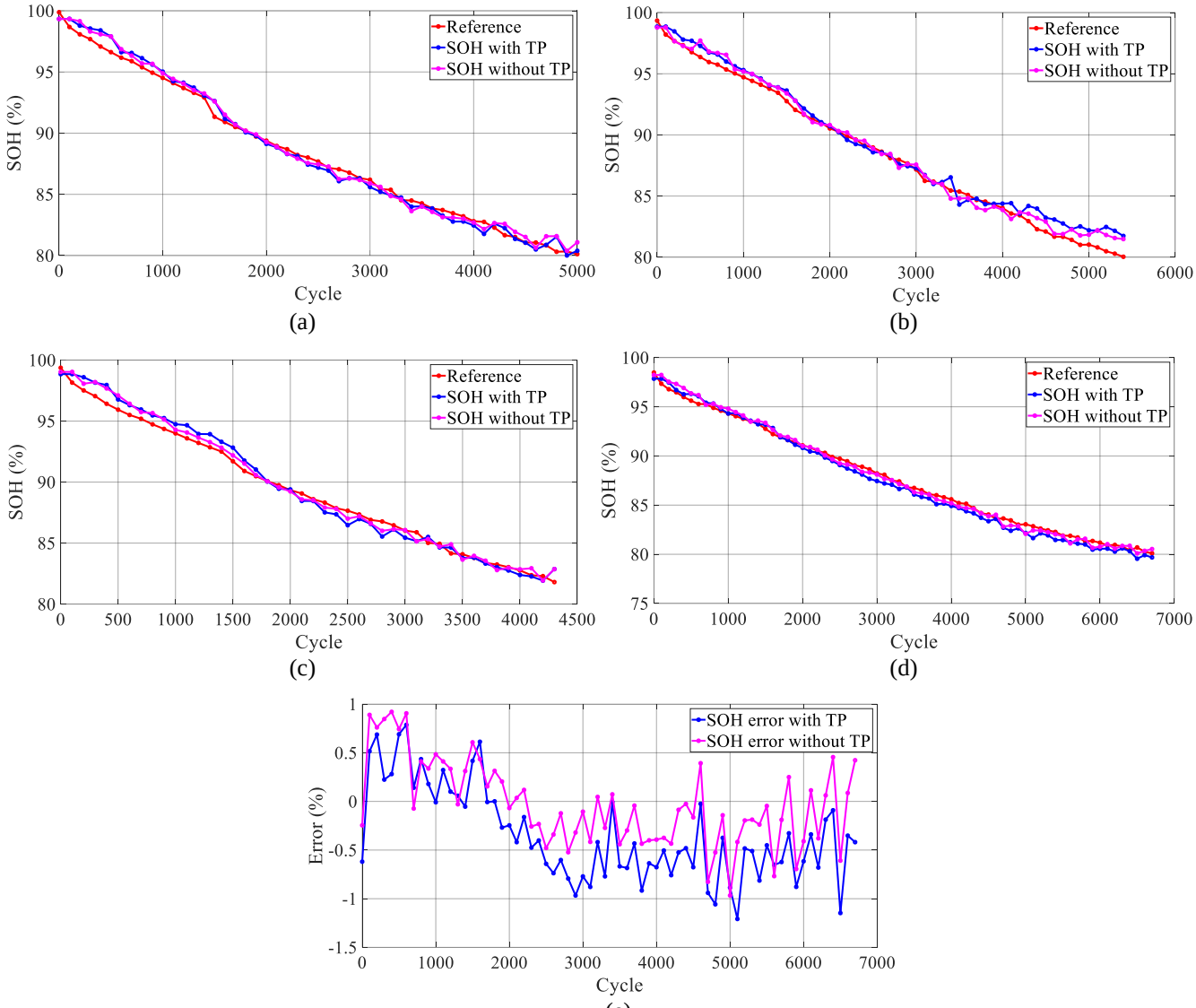

Fig. 7. SOH estimation results and errors. (a), (b), (c), and (d): the SOH estimation results of cells 1, 3, 5, and 7. (e) SOH estimation error of cell 7.

Table 6 SOH Estimation Based on Short-Term Charging Temperature

cell	RMSE (%)		MAE (%)		MAX (%)		R^2	
	with TP	without TP	with TP	without TP	with TP	without TP	with TP	without TP
1	0.58	0.58	0.47	0.47	1.32	1.28	0.9932	0.9920
2	1.20	1.02	1.02	0.82	2.28	2.41	0.9919	0.9907
3	0.83	0.64	0.66	0.51	1.99	1.45	0.9869	0.9899
4	1.14	1.14	0.98	0.95	2.01	2.41	0.9928	0.9917
5	0.72	0.57	0.62	0.47	1.54	1.26	0.9888	0.9921
6	0.93	0.74	0.78	0.60	1.75	1.62	0.9930	0.992
7	0.59	0.44	0.51	0.36	1.21	0.97	0.9959	0.9958
8	0.88	0.83	0.76	0.66	1.86	1.88	0.9926	0.9906
Average	0.86	0.74	0.73	0.61	1.75	1.66	0.9919	0.9919

C. Comparison with Different Methods

To further verify the superiority of the proposed approach, this part compares the performance of the proposed method with four classic approaches, including SVM, BP NN, Elman NN and LSTM NN. It is worth mentioning that to make fair comparisons, the hyper-parameters of LSTM NN are completely consistent with the GRU model; the hidden layer, neurons in each hidden layer, epoch of BP NN and Elman NN are the same as those of the GRU model; and the main parameters of SVM including the penalty parameter *c* and the kernel parameter *g* are carefully set to 1. The estimation results of these methods are shown in Fig. 8, where the SVM, BP NN, Elman NN and LSTM NN lead to overestimation or underestimation of SOH. By contrast, the forecasted SOH by the proposed method fluctuates near the reference value mildly and achieves better estimation, indicating that the prediction results of the proposed method can supply high-performance SOH estimation. Table 7 summarizes the SOH estimation results based on different approaches. Obviously, the estimation results by the proposed algorithm outperforms those by the remaining methods, and the LSTM NN behaves poorest among all the candidate methods. To be specific, the RMSE values by the SVM, BP NN, Elman NN and LSTM NN reach 0.69%, 0.75%, 0.79% and 1.13%, respectively. However, the RMSE supplied by the proposed approach is only 0.58% under the same case. When the proposed method is applied, the MAE is respectively reduced by 16.07%, 21.67%, 25.40% and 54.81%, compared that by the SVM, BP NN, Elman NN and LSTM NN model. Simultaneously, the MAX value by the proposed method is reduced by 29.03%, 30.53%, 34.33% and 34.98%, compared with those by the SVM, BP NN, Elman NN and LSTM NN. In addition, the R^2 of the proposed approach is 0.9932, which is higher than that of other methods visibly. Furthermore, the computational efficiency of LSTM NN and GRU NN is also compared. In this case, the total parameters of LSTM NN are 45181, and the total parameters of GRU NN are 33901. It is obvious that the number of parameters for LSTM is 1.33 times than that of GRU NN. Moreover, in the training process, the training time of LSTM NN is 190.06 s, and that of GRU NN is 176.72 s. The training time of LSTM NN is 7% more than that of GRU NN, which is enough to indicate that the calculation burden of LSTM NN is heavier than that of GRU NN. The comparison study reveals that the estimation performance of the proposed method is obviously better than that of other commonly used methods, manifesting its superiority in SOH predication.

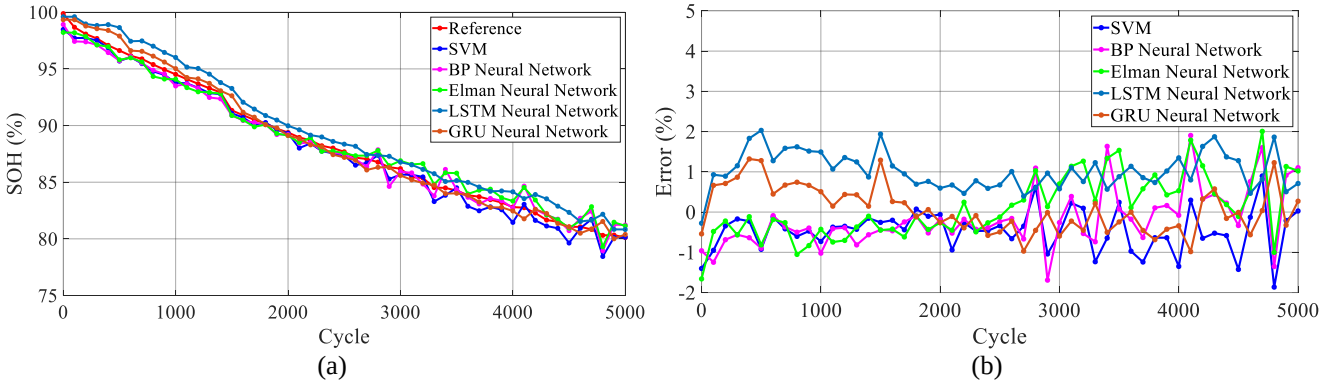

(a) (b)

Fig. 8. SOH estimation result and error of cell 1 under different methods.

Table 7 SOH Estimation of cell 1 Under Different Estimation Methods

Methods	RMSE (%)	MAE (%)	MAX (%)	R^2
SVM	0.69	0.56	1.86	0.9854
BP NN	0.75	0.60	1.90	0.9828
Elman NN	0.79	0.63	2.01	0.9809
LSTM NN	1.13	1.04	2.03	0.9625
GRU NN	0.58	0.47	1.32	0.9932

D. Discussions and Limitations

The above results validate the performance of the proposed method, but there are still some limitations and shortcomings. First, the proposed method is verified on one type of battery, and the feasibility on other types of li-ion batteries needs to be validated. Second, the algorithm is validated at high temperature (40℃), and its efficiency at other temperatures need to be further examined. When considering different temperature conditions, we only need to collect the aging data at different temperatures as the training datasets, and then the proposed method can be implemented to acquire temperature data and HFs, and conduct the model training. By this manner, the battery SOH can be estimated accurately at different temperatures. Third, this study only investigates battery cell SOH estimation and does not explore the SOH estimation of the proposed method in battery packs, and this still needs to be investigated in the future. Actually, for the battery pack, the battery thermal management system is usually designed to maintain a reasonable temperature range and minimize the temperature difference among cells [58]. Actually, our designed method can be applied to each cell in battery pack. Only if the surface temperature and the voltage can be measured or predicted, the method can be applied to predict each cell's SOH. While, the computation intensity may become larger when applying the algorithm for multiple cell's SOH estimation. How to reduce the computational burden when estimating the cells' SOH in a pack based on the proposed algorithm deserves to be further investigated.

VI. CONCLUSION

This study presents an accurate state of health estimation method based on the temperature prediction model and gated recurrent unit neural network. In the proposed method, the extreme learning machine is employed to predict the charging temperature curves by randomly discontinuous short-term charging data, and the differential temperature curves are derived by the finite difference method and then smoothed by the Kalman filter. On this basis, health features are extracted from different dimensions of the determined differential temperature curves to describe battery degradation from multiple perspectives, and six highly correlational health features are selected as the input for SOH estimation. The gated recurrent unit neural network is advanced to capture the nonlinear relationship between these selected features and state of health. Then, the accuracy and robustness of the proposed approach is fully verified by the leave-one-out validation scheme. The experimental results manifest that the proposed method can predict state of health accurately and robustly. The root-mean-square error, mean absolute error and max absolute error are constrained within 1.2%, 1.02%, and 2.28%, respectively, and the R–squared values of all cells are higher than 0.98. The validation results highlight that the proposed method can accurately estimate state of health for li-ion batteries through incomplete charging data, and shows similar performance with the raw entire temperature prediction results. Moreover, the comparison results manifest that the presented method outperforms the conventional support vector machine, backward propagation neural network, Elman neural network and long shorter-term memory neural network in terms of estimation precision and reliability. All of the experiment results expose that the developed method offers competitive and promising estimation performance in state of health prediction, thus inferring that the developed method shows the potential for practical applications.

In the future, we aim to overcome the limitations of this study, mainly by obtaining more varying and extensive datasets such as different battery types and different temperatures to train and improve the applicability, flexibility and generalization of the proposed method. Moreover, the validation of the proposed algorithm in battery pack SOH estimation also needs to be addressed.

ACKNOWLEDGEMENTS

This work was supported in part by the National Natural Science Foundation of China (No. 61763021 and 51775063), and in part by the EU-funded Marie Skłodowska-Curie Individual Fellowships Project under Grant

845102-HOEMEV-H2020-MSCA-IF-2018. The authors would like to thank them for their support and help. In addition, the authors would like to thank the anonymous reviewers for their constructive suggestions and comments.

REFERENCES

[1] X. Zhang, L. Guo, N. Guo, Y. Zou, and G. Du, "Bi-level Energy Management of Plug-in Hybrid Electric Vehicles for Fuel Economy and Battery Lifetime with Intelligent State-of-charge Reference," *Journal of Power Sources,* vol. 481, p. 228798, 2021.

[2] J. Lu, T. Wu, and K. Amine, "State-of-the-art characterization techniques for advanced lithium-ion batteries," *Nature Energy,* vol. 2, no. 3, pp. 1-13, 2017.

[3] X. Shu, G. Li, J. Shen, Z. Lei, Z. Chen, and Y. Liu, "An adaptive multi-state estimation algorithm for lithium-ion batteries incorporating temperature compensation," *Energy,* vol. 207, p. 118262, 2020.

[4] X. Li, Z. Wang, L. Zhang, C. Zou, and D. D. Dorrell, "State-of-health estimation for Li-ion batteries by combing the incremental capacity analysis method with grey relational analysis," *Journal of Power Sources,* vol. 410, pp. 106-114, 2019.

[5] H. Tian, P. Qin, K. Li, and Z. Zhao, "A review of the state of health for lithium-ion batteries: Research status and suggestions," *Journal of Cleaner Production,* vol. 261, p. 120813, 2020.

[6] T. Sun, B. Xu, Y. Cui, X. Feng, X. Han, and Y. Zheng, "A sequential capacity estimation for the lithium-ion batteries combining incremental capacity curve and discrete Arrhenius fading model," *Journal of Power Sources,* vol. 484, p. 229248, 2021.

[7] R. Xiong, L. Li, and J. Tian, "Towards a smarter battery management system: A critical review on battery state of health monitoring methods," *Journal of Power Sources,* vol. 405, pp. 18-29, 2018.

[8] W. Liu, Y. Xu, and X. Feng, "A Hierarchical and Flexible Data-Driven Method for Online State-of-Health Estimation of Li-Ion Battery," *IEEE Transactions on Vehicular Technology,* vol. 69, no. 12, pp. 14739-14748, 2020.

[9] S. Shen, M. Sadoughi, M. Li, Z. Wang, and C. Hu, "Deep convolutional neural networks with ensemble learning and transfer learning for capacity estimation of lithium-ion batteries," *Applied Energy,* vol. 260, p. 114296, 2020.

[10] X. Shu, G. Li, J. Shen, W. Yan, Z. Chen, and Y. Liu, "An adaptive fusion estimation algorithm for state of charge of lithium-ion batteries considering wide operating temperature and degradation," *Journal of Power Sources,* vol. 462, p. 228132, 2020.

[11] A. Bartlett, J. Marcicki, S. Onori, G. Rizzoni, X. G. Yang, and T. Miller, "Electrochemical model-based state of charge and capacity estimation for a composite electrode lithium-ion battery," *IEEE Transactions on control systems technology,* vol. 24, no. 2, pp. 384-399, 2015.

[12] W. Waag and D. U. Sauer, "Adaptive estimation of the electromotive force of the lithium-ion battery after current interruption for an accurate state-of-charge and capacity determination," *Applied Energy,* vol. 111, pp. 416-427, 2013.

[13] P. Li *et al.*, "State-of-health estimation and remaining useful life prediction for the lithium-ion battery based on a variant long short term memory neural network," *Journal of power sources,* vol. 459, p. 228069, 2020.

[14] Y. Zou, X. Hu, H. Ma, and S. E. Li, "Combined state of charge and state of health estimation over lithium-ion battery cell cycle lifespan for electric vehicles," *Journal of Power Sources,* vol. 273, pp. 793-803, 2015.

[15] X. Tang *et al.*, "A fast estimation algorithm for lithium-ion battery state of health," *Journal of Power Sources,* vol. 396, pp. 453-458, 2018.

[16] R. Xiong, L. Li, Z. Li, Q. Yu, and H. Mu, "An electrochemical model based degradation state identification method of Lithium-ion battery for all-climate electric vehicles application," *Applied energy,* vol. 219, pp. 264-275, 2018.

[17] M.-F. Ng, J. Zhao, Q. Yan, G. J. Conduit, and Z. W. Seh, "Predicting the state of charge and health of batteries using data-driven machine learning," *Nature Machine Intelligence,* vol. 2, no. 3, pp. 161-170, 2020.

[18] B. Liu, X. Tang, and F. Gao, "Joint estimation of battery state-of-charge and state-of-health based on a simplified pseudo-two-dimensional model," *Electrochimica Acta,* vol. 344, p. 136098, 2020/06/01/ 2020.

[19] Y. Li, Z. Wei, B. Xiong, and D. M. Vilathgamuwa, "Adaptive Ensemble-Based Electrochemical-Thermal-Degradation State Estimation of Lithium-Ion Batteries," *IEEE Transactions on Industrial Electronics,* 2021.

[20] M. Petit, E. Prada, and V. Sauvant-Moynot, "Development of an empirical aging model for Li-ion batteries and application to assess the impact of Vehicle-to-Grid strategies on battery lifetime," *Applied energy,* vol. 172, pp. 398-407, 2016.

[21] K. Li, P. Zhou, Y. Lu, X. Han, X. Li, and Y. Zheng, "Battery life estimation based on cloud data for electric vehicles," *Journal of Power Sources,* vol. 468, p. 228192, 2020.

[22] X. Hu, F. Feng, K. Liu, L. Zhang, J. Xie, and B. Liu, "State estimation for advanced battery management: Key challenges and future trends," *Renewable and Sustainable Energy Reviews,* vol. 114, p. 109334, 2019.

[23] X. Tang, C. Zou, K. Yao, J. Lu, Y. Xia, and F. Gao, "Aging trajectory prediction for lithium-ion batteries via model migration and Bayesian Monte Carlo method," *Applied Energy,* vol. 254, p. 113591, 2019.

[24] K. A. Severson *et al.*, "Data-driven prediction of battery cycle life before capacity degradation," *Nature Energy,* vol. 4, no. 5, pp. 383-391, 2019.
[25] Y. Zhang, R. Xiong, H. He, and M. G. Pecht, "Long short-term memory recurrent neural network for remaining useful life prediction of lithium-ion batteries," *IEEE Transactions on Vehicular Technology,* vol. 67, no. 7, pp. 5695-5705, 2018.
[26] X. Shu, G. Li, J. Shen, Z. Lei, Z. Chen, and Y. Liu, "A uniform estimation framework for state of health of lithium-ion batteries considering feature extraction and parameters optimization," *Energy,* vol. 204, p. 117957, 2020.
[27] X. Li, C. Yuan, X. Li, and Z. Wang, "State of health estimation for Li-Ion battery using incremental capacity analysis and Gaussian process regression," *Energy,* vol. 190, p. 116467, 2020.
[28] H. Li, D. Pan, and C. P. Chen, "Intelligent prognostics for battery health monitoring using the mean entropy and relevance vector machine," *IEEE Transactions on Systems, Man, and Cybernetics: Systems,* vol. 44, no. 7, pp. 851-862, 2014.
[29] K. S. Mawonou, A. Eddahech, D. Dumur, D. Beauvois, and E. Godoy, "State-of-health estimators coupled to a random forest approach for lithium-ion battery aging factor ranking," *Journal of Power Sources,* vol. 484, p. 229154, 2021.
[30] L. Song, K. Zhang, T. Liang, X. Han, and Y. Zhang, "Intelligent state of health estimation for lithium-ion battery pack based on big data analysis," *Journal of Energy Storage,* vol. 32, p. 101836, 2020.
[31] H. Dong, X. Jin, Y. Lou, and C. Wang, "Lithium-ion battery state of health monitoring and remaining useful life prediction based on support vector regression-particle filter," *Journal of power sources,* vol. 271, pp. 114-123, 2014.
[32] D. Yang, X. Zhang, R. Pan, Y. Wang, and Z. Chen, "A novel Gaussian process regression model for state-of-health estimation of lithium-ion battery using charging curve," *Journal of Power Sources,* vol. 384, pp. 387-395, 2018.
[33] L. Chen, H. Wang, B. Liu, Y. Wang, Y. Ding, and H. Pan, "Battery state-of-health estimation based on a metabolic extreme learning machine combining degradation state model and error compensation," *Energy,* vol. 215, p. 119078, 2021/01/15/ 2021.
[34] Z. Chen, H. Zhao, X. Shu, Y. Zhang, J. Shen, and Y. Liu, "Synthetic Stage of Charge Estimation for Lithium-ion Batteries Based on Long Short-Term Memory Network Modeling and Adaptive H-Infinity Filter," *Energy,* p. 120630, 2021.
[35] X. Shu, G. Li, Y. Zhang, S. Shen, Z. Chen, and Y. Liu, "Stage of Charge Estimation of Lithium-ion Battery Packs Based on Improved Cubature Kalman Filter with Long Short-Term Memory Model," *IEEE Transactions on Transportation Electrification,* pp. 1-1, 2020.
[36] J. Hong, Z. Wang, W. Chen, L. Wang, P. Lin, and C. Qu, "Online accurate state of health estimation for battery systems on real-world electric vehicles with variable driving conditions considered," *Journal of Cleaner Production,* vol. 294, p. 125814, 2021.
[37] S. Cui and I. Joe, "A dynamic spatial-temporal attention-based GRU model with healthy features for state-of-health estimation of lithium-ion batteries," *IEEE Access,* vol. 9, pp. 27374-27388, 2021.
[38] Y. Che, Z. Deng, X. Lin, L. Hu, and X. Hu, "Predictive battery health management with transfer learning and online model correction," *IEEE Transactions on Vehicular Technology,* vol. 70, no. 2, pp. 1269-1277, 2021.
[39] H. Zhang, J. Li, Y. Ji, and H. Yue, "Understanding subtitles by character-level sequence-to-sequence learning," *IEEE Transactions on Industrial Informatics,* vol. 13, no. 2, pp. 616-624, 2016.
[40] L. Ungurean, M. V. Micea, and G. Carstoiu, "Online state of health prediction method for lithium-ion batteries, based on gated recurrent unit neural networks," *International journal of energy research,* vol. 44, no. 8, pp. 6767-6777, 2020.
[41] L. Zheng, J. Zhu, D. D.-C. Lu, G. Wang, and T. He, "Incremental capacity analysis and differential voltage analysis based state of charge and capacity estimation for lithium-ion batteries," *Energy,* vol. 150, pp. 759-769, 2018.
[42] J. Zhu *et al.*, "Investigation of lithium-ion battery degradation mechanisms by combining differential voltage analysis and alternating current impedance," *Journal of Power Sources,* vol. 448, p. 227575, 2020.
[43] L. Wang, C. Pan, L. Liu, Y. Cheng, and X. Zhao, "On-board state of health estimation of LiFePO4 battery pack through differential voltage analysis," *Applied energy,* vol. 168, pp. 465-472, 2016.
[44] T. Shibagaki, Y. Merla, and G. J. Offer, "Tracking degradation in lithium iron phosphate batteries using differential thermal voltammetry," *Journal of Power Sources,* vol. 374, pp. 188-195, 2018.
[45] Z. Wang, C. Yuan, and X. Li, "Lithium Battery State of Health Estimation via Differential Thermal Voltammetry with Gaussian Process Regression," *IEEE Transactions on Transportation Electrification,* 2020.
[46] J. Tian, R. Xiong, and W. Shen, "State-of-Health estimation based on differential temperature for lithium ion batteries," *IEEE Transactions on Power Electronics,* vol. 35, no. 10, pp. 10363-10373, 2020.
[47] G. Huang, G.-B. Huang, S. Song, and K. You, "Trends in extreme learning machines: A review," *Neural Networks,* vol. 61, pp. 32-48, 2015.
[48] G.-B. Huang, Q.-Y. Zhu, and C.-K. Siew, "Extreme learning machine: theory and applications," *Neurocomputing,* vol. 70, no. 1-3, pp. 489-501, 2006.
[49] B. Chen, X. Liu, H. Zhao, and J. C. Principe, "Maximum correntropy Kalman filter," *Automatica,* vol. 76, pp. 70-77, 2017.

[50] S. Sharma, S. Sharma, and A. Athaiya, "Activation functions in neural networks," *International Journal of Engineering Applied Sciences and Technology,* vol. 6, no. 12, pp. 310-316, 2017.
[51] N. Srivastava, G. Hinton, A. Krizhevsky, I. Sutskever, and R. Salakhutdinov, "Dropout: a simple way to prevent neural networks from overfitting," *The journal of machine learning research,* vol. 15, no. 1, pp. 1929-1958, 2014.
[52] W. Li, N. Sengupta, P. Dechent, D. Howey, A. Annaswamy, and D. U. Sauer, "Online capacity estimation of lithium-ion batteries with deep long short-term memory networks," *Journal of Power Sources,* vol. 482, p. 228863, 2021.
[53] C. Birkl, "Diagnosis and prognosis of degradation in lithium-ion batteries," *Department of Engineering Science, University of Oxford,* 2017.
[54] F. Leng, C. M. Tan, and M. Pecht, "Effect of temperature on the aging rate of Li ion battery operating above room temperature," *Scientific reports,* vol. 5, no. 1, pp. 1-12, 2015.
[55] B. Gou, Y. Xu, and X. Feng, "State-of-health estimation and remaining-useful-life prediction for lithium-ion battery using a hybrid data-driven method," *IEEE Transactions on Vehicular Technology,* vol. 69, no. 10, pp. 10854-10867, 2020.
[56] X. Shu, G. Li, Y. Zhang, J. Shen, Z. Chen, and Y. Liu, "Online diagnosis of state of health for lithium-ion batteries based on short-term charging profiles," *Journal of Power Sources,* vol. 471, p. 228478, 2020.
[57] R. Yang, R. Xiong, W. Shen, and X. Lin, "Extreme Learning Machine-Based Thermal Model for Lithium-Ion Batteries of Electric Vehicles under External Short Circuit," *Engineering,* 2020.
[58] J. Kim, J. Oh, and H. Lee, "Review on battery thermal management system for electric vehicles," *Applied Thermal Engineering,* vol. 149, pp. 192-212, 2019/02/25/ 2019.